Rheology of a dense granular bed penetrated by a rotating impeller

Wenguang Nan [a,b], Mehrdad Pasha [b,1], Mojtaba Ghadiri [b,*]

[a] School of Mechanical and Power Engineering, Nanjing Tech University, Nanjing 211816, China
[b] School of Chemical and Process Engineering, University of Leeds, Leeds LS2 9JT, UK

ARTICLE INFO

ABSTRACT

Understanding of the rheological behaviour of fully three-dimensional and non-uniform particle flow is of great interest. We analyse the resistance exhibited by a granular bed as a rotating impeller is penetrated into it, from which the rheological characteristics of the bed are deduced. For this end, the transient rheological response of both spherical and rodlike particles is simulated by Discrete Element Method. Transition from quasi-static to intermediate flow regime of rodlike particles is found to occur at a much larger shear strain rate than that of spherical particles. The relationship between the bulk friction coefficient and the inertial number is not monotonic. The viscosity of particle flow is inferred from the blade torque and is related to the inertial number and granular temperature, for which a power law is obtained covering both quasi-static and intermediate flow regimes. It can be used for obtaining flow field in complex geometry and dynamics using continuum mechanics by Computational Fluid Dynamics.

© 2021 The Authors. Published by Elsevier B.V. This is an open access article under the CC BY license (http://creativecommons.org/licenses/by/4.0/).

1. Introduction

Dense granular flows are widely found in many industrial engineering operations, ranging from minerals, energy production from coal, pharmaceutical, foods and additive manufacturing. Besides the quasi-static characterisation of bulk powders for flow initiation, the determination of rheological properties of dense granular flow under dynamic conditions is highly desirable in order to meet requirements for manufacturing throughput. The rheological behaviour of dense granular flow is sensitive to shear strain rate, fluid medium drag and external load in addition to particle properties, such as size, density and shape. A number of instruments are available for the characterisation of bulk behaviour of dense particle flow under dynamic conditions, as recently reviewed by Ghadiri et al. [1]. Tardos and co-workers [2–4] analysed the particle flow inside a Couette device consisting of two co-axial vertical cylinders with the powder sheared in the annular gap. They showed that the particle flow could transit from the quasi-static regime to the intermediate regime, in which bulk friction and viscosity vary with the rotational speed of the inner cylinder. However, recent studies of the flow field in the co-axial Couette geometry by Nott and co-workers [5,6] has shown that despite simplicity in the device geometry, there is a secondary axial flow filed which makes the analysis complex. As an alternative to the Couette device, a rotating blade has been used to analyse the powder dynamic response to shear deformation, such as FT4 Rheometer of Freeman Technology [7] (a rotating twisted blade

penetrating into the particle bed), the powder cell of Anton Paar Modular Compact rheometer [8] and the rheometer with a blade rotating at a fixed height inside the particle bed [9–12]. In the latter two kinds of rheometers [8–12], bulk particles have largely been tested in the quasi-static regime, and the effect of shear strain rate on rheological behaviour in the intermediate regime has not been examined. In the FT4 rheometer, as the rotating impeller penetrates into the particle bed, the particle flow is fully three-dimensional transient and non-uniform. Hare et al. [13], Nan et al. [14,15] and Vivacqua et al. [16] have carried out systematic studies of the effects of cohesion, air drag and strain rate, and particle shape on particle flow by analysing the stress field of bulk particles. They identified that the flow energy (i.e. mechanical work required to drive the rotating blade into the powder bed) correlated well with the particle shear stress in front of the blade. They also confirmed that the particle flow in FT4 rheometer is transient, where normal stress changes as the impeller is penetrated into the bed. This is much different to other rheometers working with a constant normal stress, e.g. Anton Paar [8] and Polleto and co-workers' flat impeller design [9–11].

The advantage of the impeller-based rheometers is that torque can readily be measured, and as commercial instruments are available, validation by users is possible and straightforward [8–26]. However the geometry of the impeller is complex to ensure effective shearing, and therefore the dynamics of powder flow requires elaborate analysis. Previous work [13–16] has mainly focused on the local shearing region, i.e. immediately in front of the blade. For simple particle shearing flows [27–31], such as plane shearing flow and split-bottom Couette flow, the rheological behaviour has been successfully analysed by the local rheology models, developed by Jop et al. [32] and Midi [33]. However, the local rheology models are inadequate to describe systems with the

---

presence of spatial non-uniformity even for simple shearing flow, which has been attributed to a non-local effect [34]. In geometries with wall-located shear bands, such as plane shear flow [35], annular shear flow [36,37] and drum flow [38], any local concept of a yield stress would predict that the velocity field should vanish in extended domain outside the main shear band. However, slow and creeping flow could be found throughout such systems, where the stress varies below the yield stress predicted by the local rheology models. In contrast, there are also cases where particles do not flow even when the stress is above the yield limit, such as granular media down an inclined plane [39,40] as well as jamming problem in hopper flow [41] and spreading flow [42]. Recently, the analysis of non-local effects have been further extended to other kinds of systems, such as a steel ball sinking into a bucket of sand with a shear band created at the bottom of the bucket, as reported by Nichol et al. [43], and a rod moving in the gap of Couette cell, as reported by Reddy et al. [44]. However, such an analysis has not been reported so far for impeller-driven rheometers, where the particle flow is not homogeneous around the impeller and the rheological response could be affected by non-local effects. Such instruments are widely used in industry nowadays for assessing powder flowability in a comparative way. Nevertheless, little attention has been paid so far to inferring rheological properties from the same test procedure, thus enabling the prediction of powder throughput, a good example of which is screw feeders.

In this work the bulk rheological behaviour of dense particle flow is analysed by simulating the dynamic behaviour of spherical and rodlike particles in FT4 rheometer with discrete element method (DEM). The effects of shear strain rate on the transient inertial number, bulk friction coefficient and viscosity along the penetration depth have been analysed, and a mathematical model is proposed to unify the transient viscosity, where non-local effects of blade shearing are included. This provides a step towards understanding the local and non-local rheology of dense particle shearing flows, thereby producing a model of bulk friction and shear viscosity of powders for flow rate calculations.

2. Method

The dynamic behaviour of particle flow in an FT4 rheometer is simulated by DEM [45,46], where the EDEM™ software package provided by DEM Solutions, Edinburgh, UK, is used. The elastic contact force of particle-wall and interparticle interactions are described by Hertz-Mindlin contact model. The simulated system comprises a cylindrical glass vessel with 62 mm diameter and a corresponding 48 mm diameter twisted stainless steel blade, as shown in Fig. 1. The twisted blade rotates anti-clockwise and moves downward into the powder bed, resulting in compressing and shearing the bed. The rheological behaviour of spherical and rodlike shapes particles with the same volumetric particle size distribution is analysed.

The particle bed is first generated by the pluviation method, and then levelled to a pre-set height (i.e. $H_0 = 80$ mm). The volume-equivalent diameters of particles are in the range of $0.87d$-$1.13d$, with a Gaussian distribution with standard deviation of 0.1, and number-based average volume-equivalent diameter of $d = 2.0$ mm. The material properties and interaction parameters in the simulations are listed in Table 1 and Table 2, respectively. The particles in this work are large, typical of ceramic rods, and hence are treated as non-cohesive [47]. Moreover, they are under low compressive stresses, so their dynamics is not sensitive to the shear modulus. Therefore, a low shear modulus of particles is used here to speed up the simulation (Table 1). The rodlike particles are described by six clumped-spheres uniformly distributed along the major axis of the particle with hemispherical caps; the length of cylinder part L_c is equal to its diameter d_c, i.e. aspect ratio $AR = L_c/d_c = 1$, as shown in Fig. 1. The tip speed u_{tip} used in the simulation is varied from 0.025 m/s to 1.0 m/s, and the corresponding vertical downward translational velocity u and rotational velocity ω are shown in Table 3, where a helix angle of $\alpha = 5°$ is used, based on the operation of FT4 powder
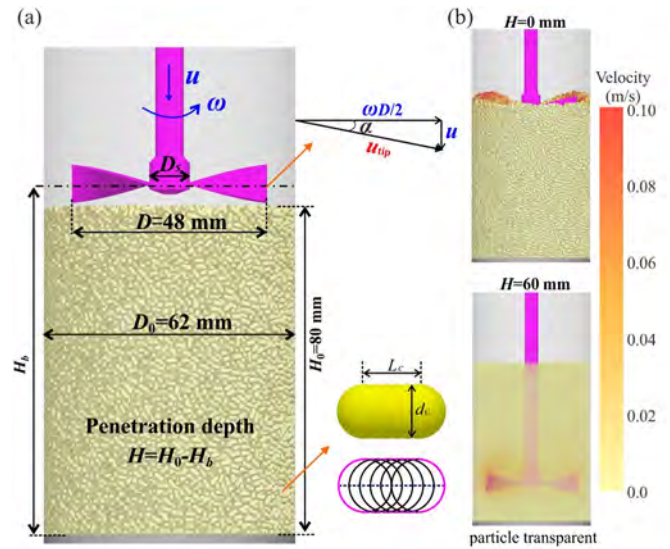

Fig. 1. Simulation set-up for FT4 powder rheometer: (a) schematic diagram, and (b) penetration process, where D_s, D and D_0 are the diameter of the shaft, blade and vessel, respectively; H_0 is the initial height of the bed, and H_b is the mid vertical position of the blade, while H is the penetration depth of the impeller; u, ω are the translational and rotational velocities of the impeller, respectively, while u_{tip} is the tip speed of the impeller and α is the helix angle; d_c and l_c are the diameter and length of the cylinder part of the rodlike particle.

Table 1
Material properties in simulations.

Material property	Particles	Blade	Vessel
Density, ρ (kg/m³)	3300	7800	2500
Shear modulus, G (Pa)	1×10^8	7.3×10^{10}	2.4×10^{10}
Poisson ratio, ν	0.3	0.3	0.3

Table 2
Contact interaction parameters in simulations.

Interaction property	Particles-particle	Particle-wall
Friction coefficient, μ	0.5	0.35
Rolling friction coefficient, μ_r	0.01	0.01
Restitution coefficient, e	0.6	0.6

Table 3
Values of the translation and rotational velocity for different tip speed.

u_{tip}, m/s	0.025	0.10	0.25	0.50	1.00
u, mm/s	2.18	8.72	21.8	43.6	87.2
ω, rad/s	1.0375	4.15	10.375	20.75	41.5

rheometer. As the rotating blade penetrates into particle bed, its penetration depth is defined as $H = H_0 - H_b$, where H_b is the mid vertical position of the blade. Thus, the initial state shown in Fig. 1(a) corresponds to a negative H, while the blade front surface is fully immersed in the bed at $H=0$, as shown in Fig. 1(b). During the penetration process, the maximum penetration depth is 64 mm.

3. Results

The particle velocity field is shown as a 'heat map' in Fig. 1(b) with the blade at $H = 60$ mm. As the blade penetrates the particle bed whist rotating, the particles close to the blade are sheared, whilst

particles remote from the blade are essentially stationary or in creeping flow. Here, three regions are used to analyse the rheological behaviour of particle flow in the rheometer: region I in front of the blade, where particles are locally sheared by the blade, as shown in Fig. 2(a), and regions II and III are laterally 90° away from the blade, where particles are in creeping flow, as shown in Fig. 2(b)-(c). Regions II and III are of the same size, but at different vertical positions, i.e. region III is directly above region II. Region II is at the mid-plane of the impeller blades. For each region, three measurement cells are considered along the radial direction on each side, where cell #1 is closest to the shaft while cell #3 is farthest away from the shaft. For each measurement cell, the circumferential depth is 8 mm, the height is the same as the blade (i.e. 10 mm), and the radial size is 6.3 mm, as shown in Fig. 2, resulting in the same volume as of cube with the size of 4 times particle diameter. In region I, the measurement cell is twisted in the same pattern as the blade, and it is 1d away from blade surface to minimise the effect of wall boundary on the calculation of particle fraction ϕ in the measurement cell, which is given as:

$$\phi = \frac{\sum\limits_{p \in V} V_p}{V} \tag{1}$$

where V_p is the volume of an individual particle; V is the volume of measurement cell. In regions II and III, the measurement cell is a flat box, and cell #1 is 1d away from the shaft surface.

The stress tensor of bulk particles in the measurement cell is given as [48]:

$$\sigma_{ij} = \frac{1}{V} \left(\sum_{p \in V} m_p \delta v_i \delta v_j + \sum_{p \in V} \sum_{c \in p} f_{p,i}{}^c \cdot r_{p,j}{}^c \right) \tag{2}$$

where

m_p is the mass of particle p; δv_i and δv_j are the fluctuation velocities of particle p; $f_{p,i}{}^c$ is the contact force at contact c of particle p, and $r_{p,j}{}^c$ is the corresponding branch vector between particle mass centre and contact point; i and j denote as X, Y or Z. Based on the stress tensor, three principal stresses are calculated: major one σ_1, intermediate one σ_2 and minor one σ_3. As the particles are large, the yield state of bulk particle flow could be described by Mohr-Coulomb criterion and Drücker-Prager criterion [49], both of which give almost the same shear stress τ with a deviation less than 5% and similar bulk friction coefficient μ_b with a deviation less than 10%, as reported by Nan et al. [12]. Here, the former is used, where for the axis-symmetric condition the normal stress P and shear stress τ are given as [12,50]:

$$P = \frac{\sigma_1 + \sigma_3}{2} \tag{3}$$

$$\tau = \frac{\sigma_1 - \sigma_3}{2} \tag{4}$$

The bulk friction coefficient μ_b at the yield state is described by the ratio of the shear stress to normal stress:

$$\mu_b = \sin\delta = \tau/P \tag{5}$$

where δ is the effective angle of internal friction. To minimise the effect of the fluctuations of bulk parameters on the results, if not specified, the data in following sections are averaged for every 5 mm penetration depth.

3.1. Shear strain rate

Shear strain rate could be roughly evaluated by the ratio of maximum particle velocity to the width of shear band, which is usually estimated to be 4 to 6 times particle diameter. In FT4 rheometer, the particle flow is fully three-dimensional and non-uniform, and the shear strain rate γ is calculated from the strain rate tensor $\boldsymbol{G}$:

$$\gamma = \sqrt{2 \sum \gamma_{ij} \gamma_{ij}} \tag{6}$$

$$\gamma_{ij} = G_{ij} - \frac{\delta_{ij}}{3} \mathrm{tr}(\boldsymbol{G}) \tag{7}$$

$$G_{ij} = \frac{1}{2} \left(\frac{\partial u_i}{\partial x_j} + \frac{\partial u_j}{\partial x_i} \right) \tag{8}$$

where $\mathrm{tr}(\boldsymbol{G})$ is the trace of strain rate tensor $\boldsymbol{G}$; δ_{ij} is Kronecker symbol; u_i and u_j are particle velocity components; x_i and x_j describe particle position; $i = 1, 2, 3$ and $j = 1, 2, 3$, where 1, 2 and 3 are the index of X, Y and Z, respectively.

Based on the mean particle position and velocity, a simplified method of velocity gradient is proposed in this work, given as:

$$\bar{u}_i = \frac{1}{N} \sum_{p \in V} u_i{}^p \tag{9}$$

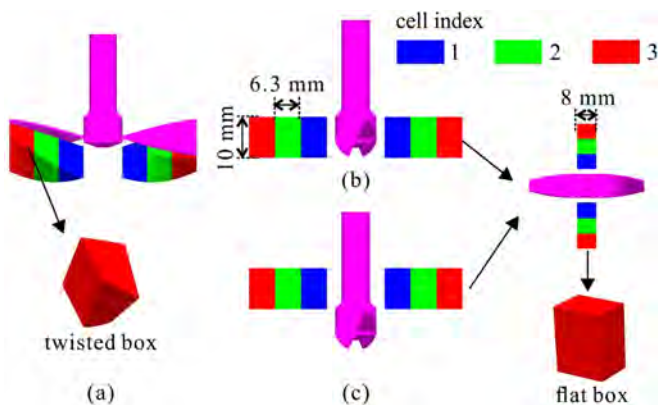$$\bar{x}_i = \frac{1}{N} \sum_{p \in V} x_i{}^p \tag{10}$$

Fig. 2. Measurement cells used for the analysis of the rheological behaviour of particle flow: (a) region I, in front of the blade, twisted boxes; (b) region II, flat boxes, the mid vertical position is the same as that of the blade; (c) region III, flat boxes, the mid vertical position is above that of the blade.
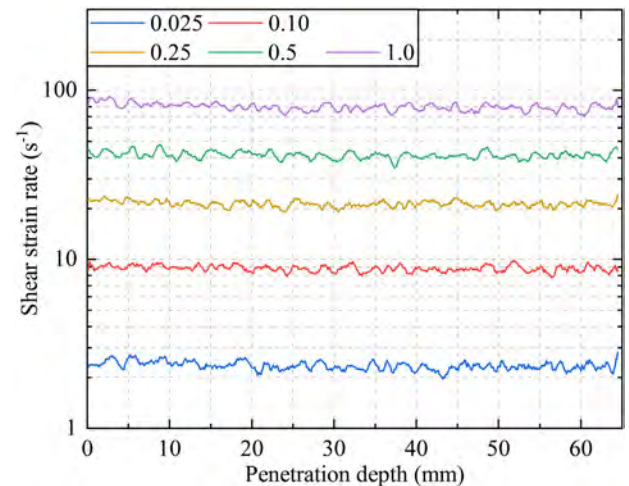

Fig. 3. Variation of cell-averaged shear strain rate γ of spherical particles with penetration depth H in region I at different tip speeds u_{tip} (m/s).

$$\frac{\partial u_i}{\partial x_j} = \frac{\sum_{p \in V}(u_i{}^p - \overline{u}_i)(x_j{}^p - \overline{x}_j)}{\sum_{p \in V}(x_j{}^p - \overline{x}_j)^2} \tag{11}$$

where N is the number of particles in the measurement cell. It produces the same results as of the more rigorous method presented in Appendix.

Fig. 3 shows the variations of cell-averaged shear strain rate with penetration depth in region I (as illustrated in Fig. 2(a)). It shows that the shear strain rate is not sensitive to the penetration depth, and it is mainly determined by the tip speed. Actually, both spherical and rodlike particles show similar shear strain rates within a deviation of 5% at the same tip speed, even in the regions far away from the blade (i.e. regions II and III), which is not shown here for simplicity. The mean cell-averaged shear strain rate is shown in Table 4, which is in the range of 0.51–82 s^{-1}. The shear strain rate varies almost linearly with the tip speed of the blade. As regions II and III are far away from the blade, the shear strain rate is much smaller than the one in region I.

The shear strain rate is normalised by the inertial timescale ($P/\rho d^2$)$^{0.5}$ to describe the inertial number, which is usually used to delineate the regime of dense granular flow [33]:

$$I = \gamma d \sqrt{\rho_p / P} \tag{12}$$

Low inertial number typically up to 0.01 indicates a quasi-static flow regime, while large inertial number in the range greater than 0.01 implies an intermediate or rapid flow regime [32,33]. Fig. 4 shows the variation of the cell-averaged inertial number with the penetration depth, which is averaged for every 5 mm penetration depth for both spherical and rodlike particles. The inertial number decreases as the impeller penetrates into the particle bed, especially for small penetration depths, mainly due to the increase of the normal stress P with the increase of penetration depth H. It also indicates that the state of particle flow may change as the blade penetrates the bed during the initial stage, where the inertial number decreases significantly, i.e. transiting from intermediate flow regime to quasi-static flow regime or becoming more quasi-static. Importantly, it also suggests that depending on the material, FT4 might measure one powder in the intermediate regime and another in the quasi-static regime.

Rodlike particles have a smaller inertial number in region I, compared to spherical particles, as they are more difficult to shear due to strong interlocking between particles. Interestingly, in region II, both particle shapes have almost the same inertial number. It indicates that particle interlocking and the strong shearing of the blade relax in this region. Although the shear strain rate is small (shown in Table 4), the inertial number is comparable to the one in region I at the same penetration depth due to small stress in region II. In both regions I and II, with the increase of tip speed, the inertial number increases as expected.

### 3.2. Rheological behaviour

Bulk flow characteristics of granular materials are commonly expressed by bulk friction and viscosity for engineering applications.

Table 4
Variation of mean cell-averaged shear strain rate with the tip speed of blade in different regions in Fig. 2.

u_{tip} (m/s)	Region	0.025	0.1	0.25	0.5	1.0
γ (s^{-1})[a]	I	2.3	8.9	22	42	82
	II	0.51	2.0	4.8	9.0	20
	III	0.56	2.0	5.0	10	25

[a] average value of spherical and rodlike particles, where they have almost the same shear strain rates at each tip speed.
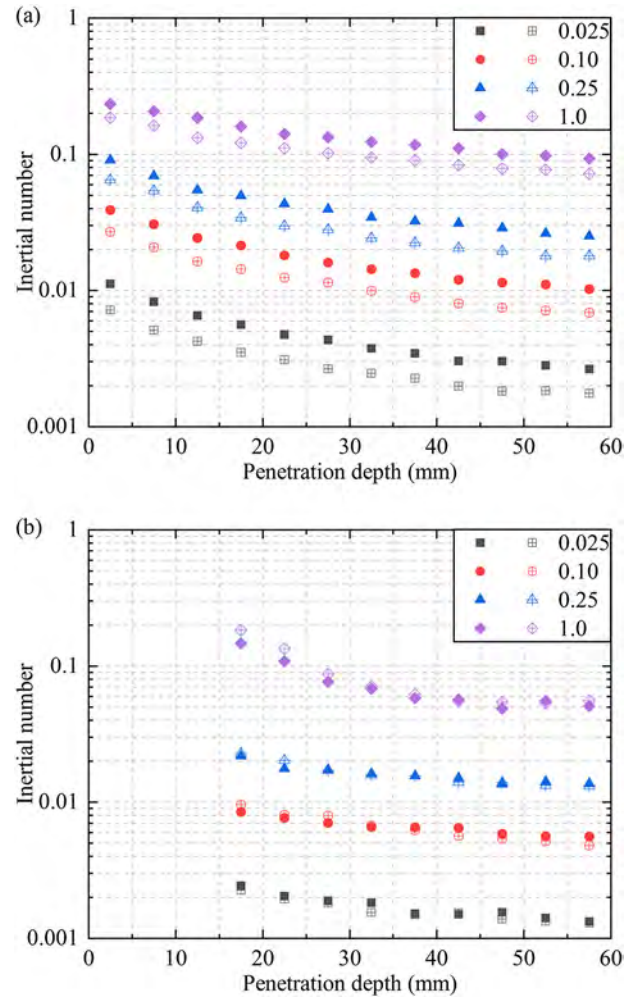
Fig. 4. Variation of cell-averaged inertial number I with penetration depth H for spherical particles (solid symbol) and rodlike particles (open symbol with cross line) at different tip speeds u_{tip} (m/s): (a) in region I (Fig. 2(a)); (b) in region II (Fig. 2(b)).

In the following these parameters are deduced from simulations of FT4 test.
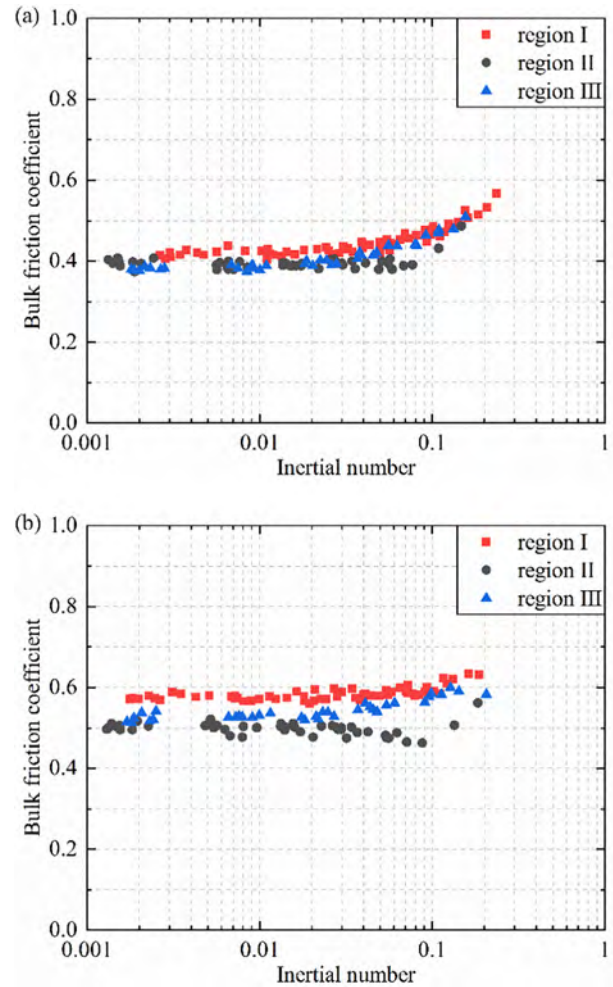
3.2.1. Bulk friction

Fig. 5 shows the variation of bulk friction coefficient with inertial number in the three measurement cells in region I, which is in front of the blade, as shown in Fig. 2(a). Each data point represents the averaged value of 5 mm penetration depth in an individual measurement cell. For spherical particles (Fig. 5 (a)), the bulk friction coefficient is constant (i.e. 0.41) when the inertial number is less than 0.02, indicating that the particle flow is in the quasi-static regime. At larger inertial numbers, the bulk friction coefficient increases with inertial number, indicating that the particle flow is in intermediate regime. Its functional form could actually be well described by a simple model [15]:

$$\mu_b = \mu_s + a(I - I_s) \tag{13}$$

where μ_s is the bulk friction coefficient in the quasi-static regime, a is the slope of $\mu_b - I$ curve, I_s is the critical value of the inertial number for transition from the quasi-static to intermediate regime. The parameters in the linear model by fitting are $a = 0.63$ and $I_s = 0.02$ and $\mu_s = 0.42$. It could also be fitted by other models, as shown and cited in Table 5, where Eqs. (13), (14) could be deemed as the simplified version of Eq. (15). Although the same value of μ_s is fitted in Eqs. (13)–(16), the
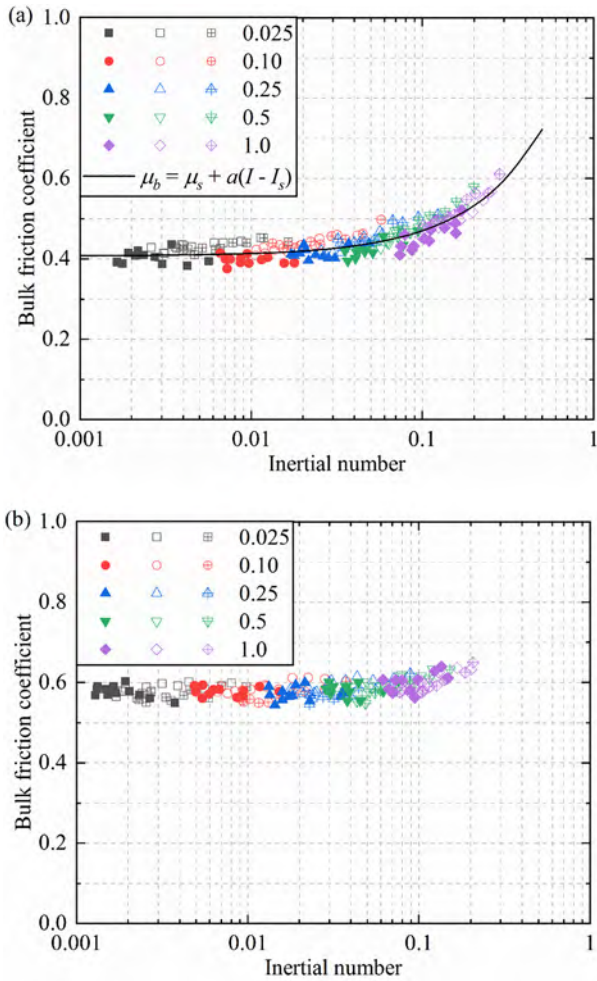
Fig. 5. Variation of bulk friction coefficient μ_b with inertial number I in region I for (a) spherical particles and (b) rodlike particles at different tip speeds u_{tip} (m/s), cell #1-solid symbol, cell #2-open symbol, cell #3-open symbol with cross line.

Fig. 6. Variation of cell-averaged bulk friction coefficient μ_b with inertial number I in the three regions for (a) spherical particles and (b) rodlike particles.

Table 5
Fitting models for bulk friction coefficient of spherical particles.

Models	Parameters			Equation number
	μ_s	a	b	
$\mu_b = \mu_s + aI$	0.41	0.63	–	Eq. (14)
$\mu_b = \mu_s + aI^b$	0.41	0.85	1.2	Eq. (15)
$\mu_b = \mu_s + \frac{a}{(b/I)^{1.5}+1}$ [15,29]	0.42	0.54	0.30	Eq. (16)

form of the dependence of μ_b on I is different when particle flow tends to intermediate flow regime.

$$\mu_b = \mu_s + aI \tag{14}$$

$$\mu_b = \mu_s + aI^b \tag{15}$$

$$\mu_b = \mu_s + \frac{a}{(b/I)^{1.5}+1} \tag{16}$$

For rodlike particles, the bulk friction coefficient in the quasi-static regime is larger than that of spherical particles, as discussed by Nan et al. [51]. Fig. 5 (b) shows that the bulk friction coefficient starts

increasing when the inertial number is larger than 0.1. This corresponds to small penetration depth at $u_{tip} = 1.0$ m/s. However, the transition from quasi-static to intermediate regimes of rodlike particles occurs at much larger shear strain rate γ (i.e. larger inertial number I) than that of spherical particles. Interestingly, Fig. 5 also indicates that different flow regimes prevail as the blade penetrates into the particle bed at a set tip speed. For example, at $u_{tip} = 0.25$ m/s for spherical particles and $u_{tip} = 1.0$ m/s for rodlike particles, the bulk friction coefficient at small penetration depths (i.e. large inertial number) is larger than the one at large penetration depths (i.e. small inertial number), and in the range that indicates the particle flow is initially in intermediate regime and then transits to quasi-static flow regime with the penetration of the rotating blade. This has important practical implications for powder flow characterisation.

Fig. 6 shows the variation of the cell-averaged bulk friction coefficient with the inertial number in the three regions. The bulk friction coefficient in regions II and III, which are well away from the impeller blade, is smaller than that in region I. It suggests that at the same inertial number, particles could flow even when the stress varies below the yield stress predicted by the local rheology models. Clearly, the bulk friction coefficient is not unified for the three regions in this form. Thus, μ_b predicted from the framework of local rheology [32] or Eqs. (13)–(16) in this work cannot satisfactorily predict the particle flow far away from the blade, which is usually perceived as nonlocal effects. Fig. 6
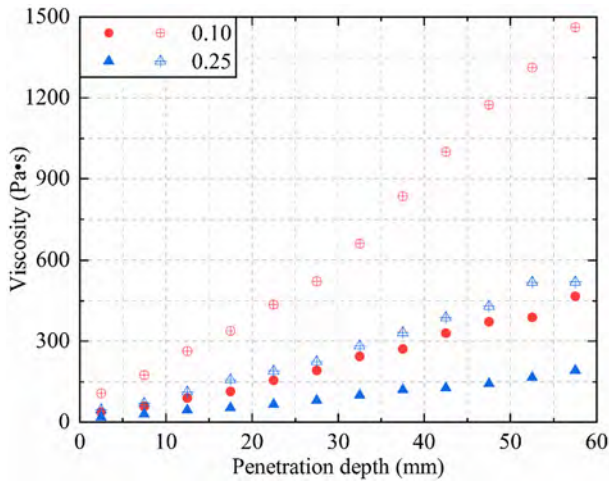
Fig. 7. Variation of cell-averaged viscosity η with penetration depth H in region I for spherical particles (solid symbol) and rodlike particles (open symbol with cross line) at different tip speeds u_{tip} (m/s).
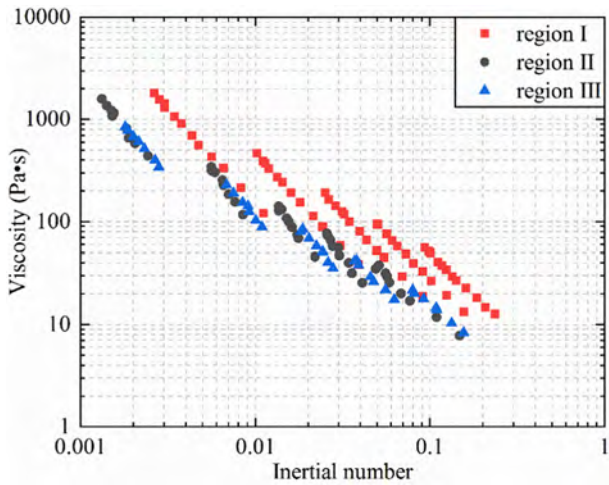

Fig. 8. Variation of cell-averaged viscosity η with inertial number I in the three regions for spherical particles; in each region, each family of lines corresponds to one blade tip speed u_{tip}, i.e. 0.05 m/s, 0.1 m/s, 0.25 m/s, 0.5 m/s and 1.0 m/s, from left to right.

also shows that the non-local effects of rodlike particles are stronger than that of spherical particles.

3.2.2. Bulk viscosity

In analogy with liquids, the rheology of particle flow is commonly described by the viscosity $\eta = \tau/\gamma$, i.e. the resistance of shear deformation rate expressed by the ratio of the shear stress to the deformation rate. Fig. 7 shows the variation of cell-averaged viscosity in region I as the impeller penetrates into the particle bed. The viscosity increases with the penetration depth, indicating that the particle bed becomes more resistant to blade shearing at large penetration depths. Rodlike particles have a much larger viscosity than spherical particles at the same penetration depth due to interlocking. The variation of viscosity with the inertial number is shown in Fig. 8, indicating a shear-thinning behaviour. For a given blade tip speed, e.g. 0.1 m/s, as the impeller is penetrated into the bed, i.e. the inertial number decreasing, the viscosity increases in a straight line on log-log plot. Families of lines like this are obtained for other blade tip speeds. As the tip speed is increased from 0.1 m/s to 0.5 m/s (i.e. increasing inertial number), the data points for each penetration move right as a line. A linear

trend clearly prevails between the viscosity and inertial number in logarithmic coordinates, suggesting a power law relationship similar to the case of shear-thinning liquids [52] for which viscosity is a power law function of the shear strain rate, i.e. $\eta = k\gamma^n$:

$$\eta = kI^n \tag{17}$$

However, distinctively different from shear-thinning liquids, the shear stress in bulk particle systems depends directly on the normal stress. Thus, the inertial number, comprising the shear strain rate and normal stress, better describes the rheology of granular flow than the strain rate. The power index, n, is in the range of -2 to -1, as obtained from fitting the results in this work (not shown here for simplicity). This could be contrasted with the range of n of shear-thinning liquids, which is typically between 0 (Newtonian liquid) and -1 (very non-Newtonian liquid).

The distinct difference of the family of lines for region I from those of the other two regions in Fig. 8 might have arisen from collisional dynamics in the former and sustained sliding contacts for the latter. It is therefore of interest to explore the influence of granular temperature T, according to the kinetic theory [53], where the viscosity is normalised by the granular temperature T:
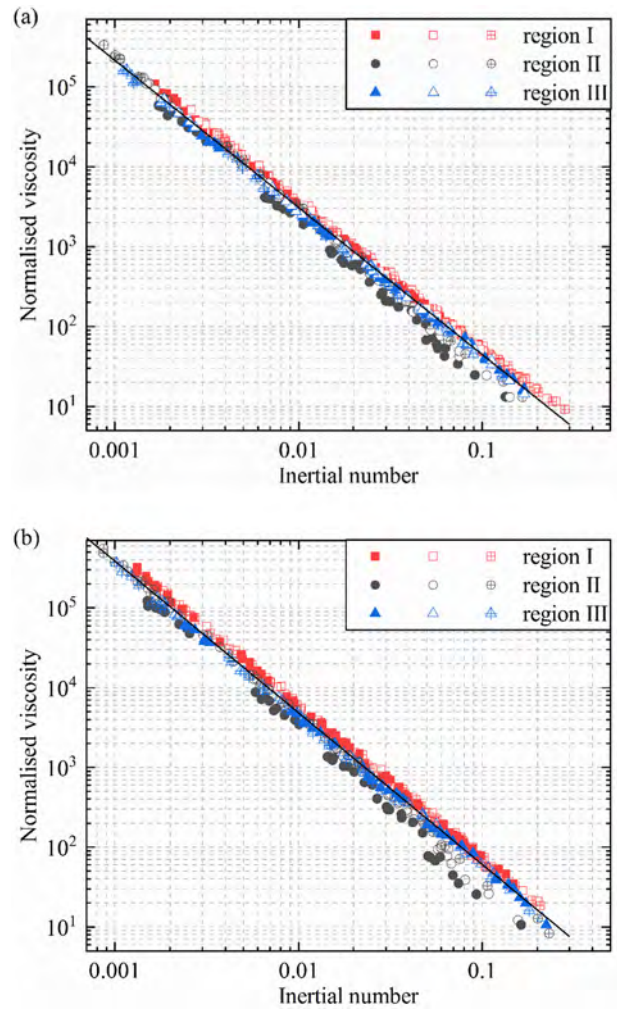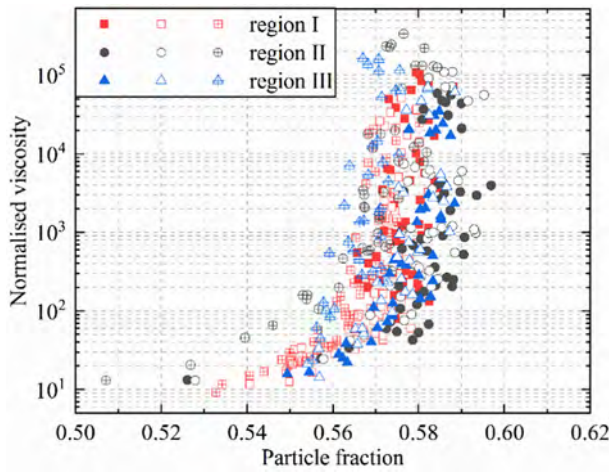
$$\eta^* = \frac{\eta}{\rho d\sqrt{T}} \tag{18}$$

Fig. 9. Variation of normalised viscosity η^* with inertial number I in three measurement cells for (a) spherical particles and (b) rodlike particles, cell #1-solid symbol, cell #2-open symbol, cell #3-open symbol with cross line.

Fig. 10. Variation of normalised viscosity η^* with particle fraction ϕ for spherical particles, cell #1-solid symbol, cell #2-open symbol, cell #3-open symbol with cross line.

$$T = \frac{1}{3N} \sum_{p \in V} \sum_{i=1,2,3} (u_i^p - \overline{u}_i)^2 \qquad (19)$$

The variation of normalised viscosity with inertial number is shown in Fig. 9. A linear trend is found on logarithmic coordinates, and all 420 data points almost collapse to one line, which is given as:

$$\eta^* = aI^{b-2} \qquad (20)$$

For spherical particles, $a = 0.65$ and $b = 0.16$, while for rodlike particles, $a = 0.77$ and $b = 0.1$, by using linear regression. η^* is larger for rodlike particles as compared with spherical particles at the same inertial number, indicating more resistance to shear deformation rate. Similar trend could also be obtained if local bulk density (i.e. $\rho\phi$) is used in Eq. (18), which is not shown here for brevity.

It should be noted that in the above scaling, η^* depends mainly on the inertial number, which is different to the original ones in the kinetic theory of rapid flow (where η^* only depends on particle fraction, see Andreotti et al. [48]). Fig. 10 shows the variation of normalised viscosity η^* with particle fraction, where a sharp increase with the increase of particle fraction is observed, indicating that a small variation of particle fraction could lead to dramatic changes of η^*. Meanwhile, a large spread of the data points is found. Thus, η^* could not be well described by local particle fraction of dense particle flow alone considered in this work.

3.2.3. Bulk viscosity inferred from blade torque

From an engineering view point, it is of great interest to infer the bulk viscosity from impeller torque measurements. As the rotating impeller penetrates into the particle bed, the transient vertical force F_b and rotating torque T_b on the blade are recorded. In FT4 rheometer, the total input mechanical work E is calculated for the torque and downward force:

$$E = \int_0^H \left(\frac{T_b}{R \tan \alpha} + F_b \right) dH \qquad (21)$$

where R is the blade radius, i.e. $D/2$ in Fig. 1. The variation of E with the penetration depth H is shown in Fig. 11, obtained from simulations of spherical and rodlike particles. This has in fact been validated previously for the same system by observing a good agreement between simulation predictions and experimental results [13,15,23,51], and hence not presented here for brevity. The total input work increases with the penetration depth in a power law form for both particle systems. Its value for any penetration depth is larger for the rodlike particle as compared to spherical ones by a factor of around 2. For spherical particles, when
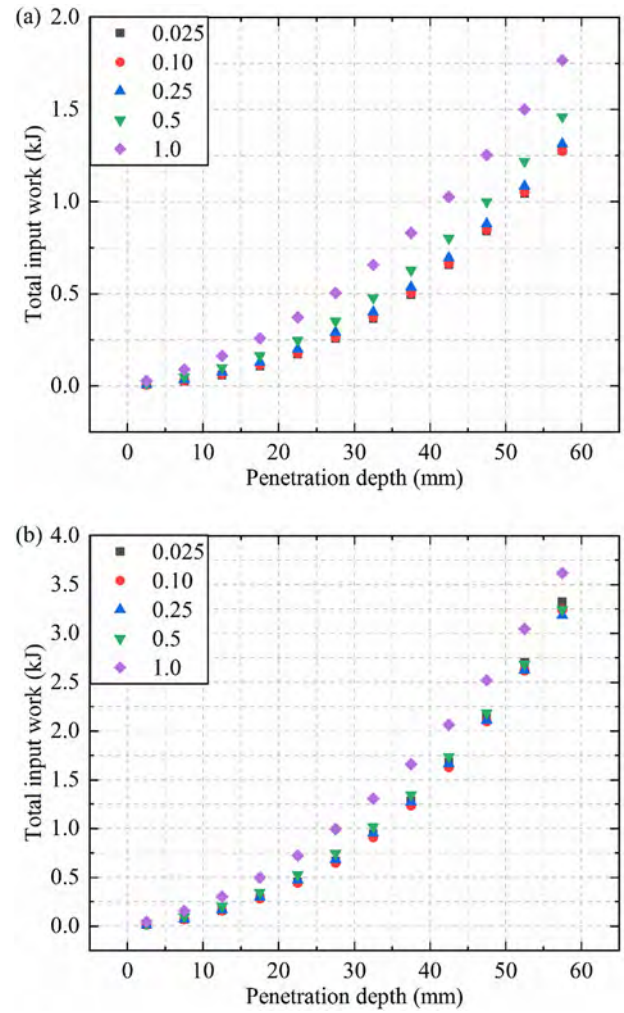
Fig. 11. Simulation prediction of total input work E as a function of penetration depth H at different tip speeds u_{tip} (m/s) for (a) for spherical particles and (b) rodlike particles.

the tip speed is less than 0.25 m/s, the total input work varies little with the tip speed at a given penetration depth, indicating that the particle flow is in quasi-static regime. For rodlike particles, the data points overlap even for the tip speed of 0.5 m/s, indicating that the particle flow transfers from quasi-static to intermediate flow regimes at larger tip speeds, as compared to the spherical particles, i.e. increasing from 0.5 m/s to 1.0 m/s. This suggests that the total input work is related to the flow regime in the rheometer. However, it should also be noted that as the total input work is the accumulation of contributions of the transient force and torque along the penetration depth, the fluctuations from transient force and torque are smoothed out by integration. Therefore, the transient state of particle flow could be better described in differential form of the input work.

The blade torque contributes about 85% of the total input work at any penetration depth and is attributed to the shear resistance (i.e. shear stress) in front of the blade. Thus, characteristic linear shear stress density $l_e \tau_e$ could be estimated from the impeller torque, as reported by Nan et al. [12], and the characteristic viscosity of particle flow is given as:

$$\eta_e = \frac{T_b}{D^2 l_e \gamma} \qquad (22)$$

where D is the blade diameter shown in Fig. 1; l_e is the equivalent action length of characteristic shear stress τ_e in the circumferential direction
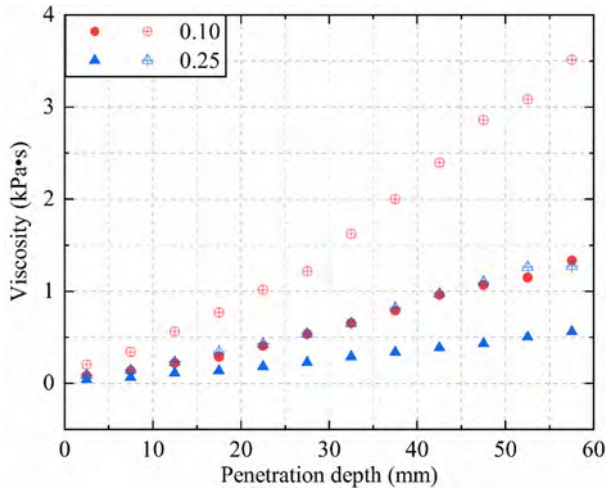
Fig. 12. Variation of viscosity η_e with penetration depth H for spherical particles (solid symbol) and rodlike particles (open symbol with cross line) at different tip speeds u_{tip} (m/s).
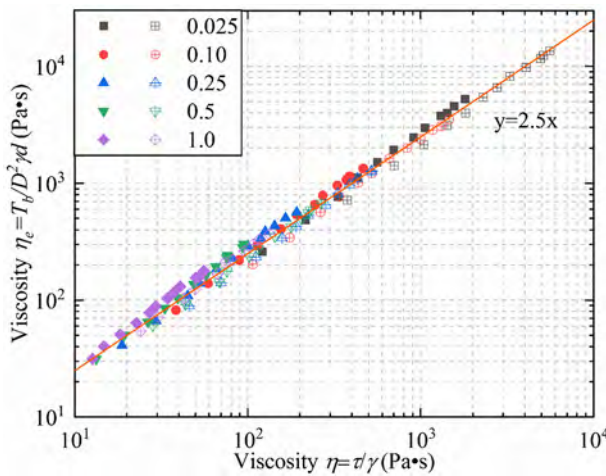

Fig. 13. Variation of η_e with $\eta = \tau/\gamma$ in region I for spherical particles (solid symbol) and rodlike particles (open symbol with cross line) at different tip speeds u_{tip} (m/s).

Fig. 14. Variation of normalised viscosity η_1 (i.e. inverse of normalised fluidity, Eq. (23)) with particle fraction ϕ for (a) spherical particles and (b) rodlike particles, where cell-averaged value is used.

[12]. l_e is expressed as λd here for simplicity, where λ is a non-dimensional factor. The variation of viscosity η_e with the penetration depth is shown in Fig. 12. The viscosity increases with the penetration depth, and the rodlike particles have a larger viscosity than that of spherical particles. It is worthwhile comparing the predicted viscosity from the two approaches for region I analysed here, i.e. from $\eta = \tau/\gamma$ and Eq. (22), as shown in Fig. 7 and Fig. 12, respectively. This is shown in Fig. 13. A good correlation is noted, as the impeller torque is mainly affected by the shear resistance in front of the blades (region I), whilst the contributions of shear resistance far away from the blades is much smaller. This suggests that the viscosity η of bulk particles in the rheometer could be inferred from the blade torque. All the 120 data points collapse to one line, for the case when the characteristic value of λ is 2.5, as shown by the slope of the line. It should be noted that $\eta_e = T_b/(\lambda D^2\gamma d)$ should be viewed as a characteristic viscosity, as λ depends on rheometer geometry and particle material properties.

4. Discussion

The results presented above indicate that the rheological characteristics of a bed of particles penetrated by a rotating impeller may be
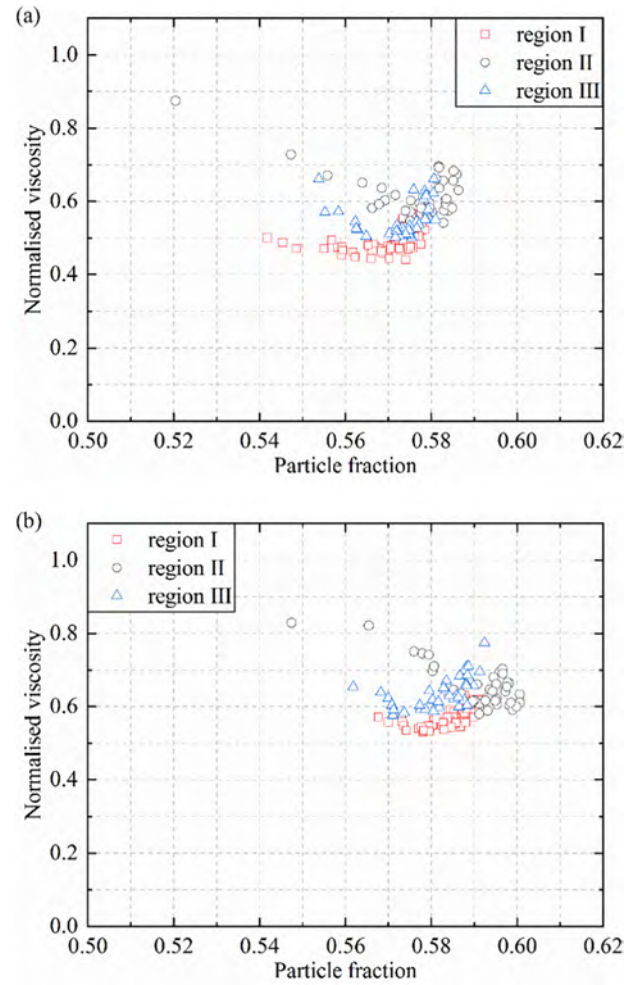
described in terms of viscosity-inertial number functional form. With reference to Eq. (18), Losert et al. [54] propose another scaling method for the viscosity of dense particle flow:

$$\eta_1 = \frac{\eta}{Pd/\sqrt{T}} \tag{23}$$

According to the following derivation, η_1 could be deemed as the inverse of normalised granular fluidity proposed by Zhang and Kamrin [55]:

$$\eta_1 = \frac{\tau/\gamma}{Pd/\sqrt{T}} = \frac{\tau/P}{\gamma d/\sqrt{T}} = \frac{\mu}{\gamma d/\sqrt{T}} = \frac{1}{g d/\sqrt{T}} \tag{24}$$

where g is granular fluidity proposed by Kamrin and Koval [37]:

$$g = \frac{\gamma}{\mu} = \frac{1}{\eta P} \tag{25}$$

Zhang and Kamrin [55] view granular fluidity as a kinematic variable, given by the granular temperature and packing fraction, by using the kinetic theory [53] of rapid granular flow and Eyring's transition state theory for liquids [56]. However, their derivation involves several hypotheses, such as $P = \rho T^{0.5}F(\phi)$, and the shearing process is described

by shear strain rate and granular temperature, where the effect of external load (i.e. P) is omitted, i.e. imbedded in the packing function. Zhang and Kamrin [55] show that the normalised granular fluidity (i.e. $gdT^{0.5}$ or $1/\eta_1$) is a monotonic function of particle fraction in uniform shear flow of spherical particles. This is not observed here as shown in Fig. 14, especially for rodlike particles, even though the data are very scattered. Furthermore, η_1 (inverse of normalised granular fluidity) is also found scattered with the variation of inertial number, which is not shown here for brevity. Thus, compared to the scaling method in Eq. (23) or normalised granular fluidity of Zhang and Kamrin [55], the scaling method given in Eq. (18) is simpler and fitting the data well, and hence more attractive for the particle flow induced by a moving impeller. Thus, using DEM simulations, a general constitutive equation is proposed for granular flow, i.e. $\eta/(\rho dT^{0.5}) = f(I)$, relating three dimensionless variables: η, T and I. The function $f(I)$ has a certain general form, i.e. $f(I) = aI^{b-2}$, for which the model parameters depend on the material properties and most importantly they can be deduced from experimental measurements of the torque from an impeller-driven rheometer. The above analysis provides a model of bulk friction and viscosity, which can be used for obtaining flow field for complex geometry and dynamics using continuum mechanics by Computational Fluid Dynamics. The outcome also suggests that in the rheology of granular flow the granular temperature should be included, which accounts for momentum diffusion outside the shear zone, as denoted by the term non-local effect in granular flow.

5. Conclusions

The rheological behaviour of a fully three-dimensional and non-uniform particle flow, induced by an impeller with twisted blades penetrating into the particle bed while rotating anti-clockwise, has been analysed using DEM simulations. The effects of penetration depth and blade tip speed on the shear strain rate, bulk friction coefficient and viscosity are examined for two particle shapes, spherical and rodlike. The main results from the present study are summarised as follows:

1) Two new methods are proposed to calculate the shear strain rate. It is found that shear strain rate is insensitive to penetration depth and particle shape. As the impeller moves downward, the pressure increases and hence the inertial number decreases. An important consequence is that different flow regimes may prevail, giving rise to the bulk friction coefficient and shear viscosity varying with depth.

2) Transition from quasi-static to intermediate regime of rodlike particles requires a much larger shear strain rate than that of spherical particles. The bulk friction coefficient, μ_b, is not unified for the three regions considered in this work, and thus the framework of local rheology model cannot satisfactorily predict the particle flow far away from the blade.

3) The viscosity of particle flow is inferred from the impeller torque and is related to the inertial number and granular temperature, for which a unified power law model is obtained covering both quasi-static and intermediate flow regimes. The model can be used for obtaining flow field in complex geometry and dynamics using continuum mechanics by Computational Fluid Dynamics.

Declaration of Competing Interest

The authors declare that they have no known competing financial interests or personal relationships that could have appeared to influence the work reported in this paper.

Appendix A. Appendix

The velocity gradient used in Eq. (8) could rigorously be calculated based on a pair of particles (i.e. particles p and q), where their spatial positions should meet the following criteria to avoid strong fluctuations due to contact or correlated motion (i.e. particle p is next to q):

$$|x_{p,i} - x_{q,i}| > d \tag{A1}$$

$$\sqrt{\sum_{i=1,2,3} \left(x_{p,i} - x_{q,i}\right)^2} < 4d \tag{A2}$$

The velocity gradient is then given as:

$$\frac{\partial u_i}{\partial x_j} = \frac{1}{N_{pair}} \sum_{p=1}^{N-1} \sum_{q=p+1}^{N} \frac{u_{p,i} - u_{q,i}}{x_{p,j} - x_{q,j}} \tag{A3}$$

where N_{pair} is the number of particle pair meeting the criteria in Eqs. (A1) and (A2). The comparison between this rigorous method and the simplified method (i.e. Eqs. (9)–(11)) is shown in Fig. 15. Both methods give almost the same shear strain rate. Thus, the method based on the mean particle position and velocity is used in this work due to its simple form and less computational time.
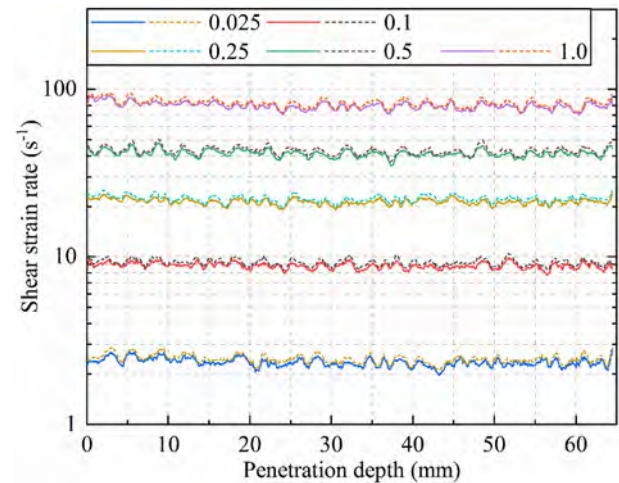

Fig. 15. Comparisons between two calculation methods of shear strain rate γ as a function of penetration depth H for different tip speeds u_{tip} (m/s): the rigorous method based on particle pair (dotted line), the simplified method based on averaged particle position and velocity (solid line).

References

[1] M. Ghadiri, M. Pasha, W.G. Nan, C. Hare, V. Vivacqua, U. Zafar, S. Nezamabadi, A. Lopez, M. Pasha, S. Nadimi, Cohesive powder flow: trends and challenges in characterisation and analysis, Kona Powd. Part. J. 37 (2020) 3–18.

[2] G.I. Tardos, S. McNamara, I. Talu, Slow and intermediate flow of a frictional bulk powder in the Couette geometry, Powder Technol. 131 (2003) 23–39.

[3] M.K. Langroudi, S. Turek, A. Ouazzi, G.I. Tardos, An investigation of frictional and collisional powder flows using a unified constitutive equation, Powder Technol. 197 (2010) 91–101.

[4] M. Kheiripour Langroudi, P.R. Mort, G.I. Tardos, Study of powder flow patterns in a Couette cell with axial flow using tracers and solid fraction measurements, Granul. Matter 13 (2011) 541–552.

[5] K.P. Krishnaraj, P.R. Nott, A dilation-driven vortex flow in sheared granular materials explains a rheometric anomaly, Nat. Commun. 7 (2016) 1–8.

[6] V. Mehandia, K.J. Gutam, P.R. Nott, Anomalous stress profile in a sheared granular column, Phys. Rev. Lett. 109 (2012) 128002.

[7] R. Freeman, Measuring the flow properties of consolidated, conditioned and aerated powders — a comparative study using a powder rheometer and a rotational shear cell, Powder Technol. 174 (2007) 25–33.

[8] H. Salehi, D. Barletta, M. Poletto, D. Schütz, R. Romirer, On the use of a powder rheometer to characterize the powder flowability at low consolidation with torque resistances, AICHE J. 63 (2017) 4788–4798.

[9] G. Bruni, D. Barletta, M. Poletto, P. Lettieri, A rheological model for the flowability of aerated fine powders, Chem. Eng. Sci. 62 (2007) 397–407.

[10] G. Bruni, A. Colafigli, P. Lettieri, T. Elson, Torque measurements in aerated powders using a mechanically stirred fluidized bed rheometer (msFBR), Chem. Eng. Res. Des. 83 (2005) 1311–1318.

[11] I. Tomasetta, D. Barletta, P. Lettieri, M. Poletto, The measurement of powder flow properties with a mechanically stirred aerated bed, Chem. Eng. Sci. 69 (2012) 373–381.

[12] W.G. Nan, Y.Q. Gu, Stress analysis of blade Rheometry by DEM simulations, Powder Technol. 376 (2020) 332–341.

[13] C. Hare, U. Zafar, M. Ghadiri, T. Freeman, J. Clayton, M.J. Murtagh, Analysis of the dynamics of the FT4 powder rheometer, Powder Technol. 285 (2015) 123–127.

[14] W.G. Nan, V. Vivacqua, M. Ghadiri, Y.S. Wang, Numerical analysis of air effect on the powder flow dynamics in the FT4 powder rheometer, EPJ Web Conf. 140 (2017), 03036.

[15] W.G. Nan, M. Ghadiri, Y.S. Wang, Analysis of powder rheometry of FT4: effect of air flow, Chem. Eng. Sci. 162 (2017) 141–151.

[16] V. Vivacqua, A. López, R. Hammond, M. Ghadiri, DEM analysis of the effect of particle shape, cohesion and strain rate on powder rheometry, Powder Technol. 342 (2019) 653–663.

[17] R. Bharadwaj, W.R. Ketterhagen, B.C. Hancock, Discrete element simulation study of a Freeman powder rheometer, Chem. Eng. Sci. 65 (2010) 5747–5756.

[18] M. Leturia, M. Benali, S. Lagarde, I. Ronga, K. Saleh, Characterization of flow properties of cohesive powders: a comparative study of traditional and new testing methods, Powder Technol. 253 (2014) 406–423.

[19] Z. Yan, S.K. Wilkinson, E.H. Stitt, M. Marigo, Investigating mixing and segregation using discrete element modelling (DEM) in the Freeman FT4 rheometer, Int. J. Pharm. 513 (2016) 38–48.

[20] C. Hare, M. Ghadiri, Stress and strain rate analysis of the FT4 powder rheometer, EPJ Web Conf. 140 (2017), 03034.

[21] S.K. Wilkinson, S.A. Turnbull, Z. Yan, E.H. Stitt, M. Marigo, A parametric evaluation of powder flowability using a Freeman rheometer through statistical and sensitivity analysis: a discrete element method (DEM) study, Comput. Chem. Eng. 97 (2017) 161–174.

[22] M. Li, M. Leturia, K. Saleh, Analysis of the periodic motion in a powder rheometer and development of a new flowability testing method, KONA Powd. Part. J. 35 (2018) 160–171.

[23] M. Pasha, N.L. Hekiem, X. Jia, M. Ghadiri, Prediction of flowability of cohesive powder mixtures at high strain rate conditions by discrete element method, Powder Technol. 372 (2020) 59–67.

[24] D. Barletta, G. Donsi, G. Ferrari, M. Poletto, A rotational tester for the characterization of aerated shear flow of powders, Part. Part. Syst. Charact. 24 (2007) 259–270.

[25] H. Salehi, D. Sofia, D. Schütz, D. Barletta, M. Poletto, Experiments and simulation of torque in Anton Paar powder cell, Part. Sci. Technol. 36 (2018) 501–512.

[26] L.A.A. Yahia, T.M. Piepke, R. Barrett, A. Ozel, R. Ocone, Development of a virtual Couette rheometer for aerated granular material, AICHE J. 66 (2020).

[27] G. Koval, J.N. Roux, A. Corfdir, F. Chevoir, Annular shear of cohesionless granular materials: from the inertial to quasistatic regime, Phys. Rev. E Stat. Nonlinear Soft Matter Phys. 79 (2009) 021306.

[28] F. da Cruz, S. Emam, M. Prochnow, J.N. Roux, F. Chevoir, Rheophysics of dense granular materials: discrete simulation of plane shear flows, Phys. Rev. E Stat. Nonlinear Soft Matter Phys. 72 (2005) 021309.

[29] S. Chialvo, J. Sun, S. Sundaresan, Bridging the rheology of granular flows in three regimes, Phys. Rev. E Stat. Nonlinear Soft Matter Phys. 85 (2012) 021305.

[30] S. Luding, Constitutive relations for the shear band evolution in granular matter under large strain, Particuology 6 (2008) 501–505.

[31] A. Singh, V. Magnanimo, K. Saitoh, S. Luding, The role of gravity or pressure and contact stiffness in granular rheology, New J. Phys. 17 (2015), 043028.

[32] P. Jop, Y. Forterre, O. Pouliquen, A constitutive law for dense granular flows, Nature 441 (2006) 727–730.

[33] G.D.R. MiDi, On dense granular flows, Eur. Phys. J E Soft Matter. 14 (2004) 341–365.

[34] K. Kamrin, Non-locality in granular flow: phenomenology and modeling approaches, Front. Phys. 7 (2019) 1–7.

[35] F. Radjai, P. Rognon, P. Kharel, T. Miller, I. Einav, S. Nezamabadi, S. Luding, J.Y. Delenne, How granular vortices can help understanding rheological and mixing properties of dense granular flows, EPJ Web Conf. 140 (2017), 03044.

[36] Z. Tang, T.A. Brzinski, M. Shearer, K.E. Daniels, Nonlocal rheology of dense granular flow in annular shear experiments, Soft Matter 14 (2018) 3040–3048.

[37] K. Kamrin, G. Koval, Nonlocal constitutive relation for steady granular flow, Phys. Rev. Lett. 108 (2012) 178301.

[38] I. Govender, Granular flows in rotating drums: a rheological perspective, Miner. Eng. 92 (2016) 168–175.

[39] K. Kamrin, D.L. Henann, Nonlocal modeling of granular flows down inclines, Soft Matter 11 (2015) 179–185.

[40] O. Pouliquen, Y. Forterre, A non-local rheology for dense granular flows, Philos. Trans. A Math Phys. Eng. Sci. 367 (2009) 5091–5107.

[41] R.P. Behringer, Dynamics and Rheology of Cohesive and Deformable Granular Materials, Jamming and Flow in a Hopper, Initial Report, IFPRI Grant 56_01, 2007 1–3.

[42] W.G. Nan, M. Pasha, T. Bonakdar, A. Lopez, U. Zafar, S. Nadimi, M. Ghadiri, Jamming during particle spreading in additive manufacturing, Powder Technol. 338 (2018) 253–262.

[43] K. Nichol, A. Zanin, R. Bastien, E. Wandersman, M. van Hecke, Flow-induced agitations create a granular fluid, Phys. Rev. Lett. 104 (2010), 078302.

[44] K.A. Reddy, Y. Forterre, O. Pouliquen, Evidence of mechanically activated processes in slow granular flows, Phys. Rev. Lett. 106 (2011) 108301.

[45] P.A. Cundall, O.D.L. Strack, A discrete numerical model for granular assemblies, Géotechnique 29 (1979) 47–65.

[46] C. Thornton, Granular Dynamics, Contact Mechanics and Particle System Simulations, Springer, New York, 2015.

[47] D. Geldart, N. Harnby, A.C. Wong, Fluidization of cohesive powders, Powder Technol. 37 (1984) 25–37.

[48] B. Andreotti, Y. Forterre, O. Pouliquen, Granular Media: Between Fluid and Solid, Cambridge University Press, 2013.

[49] K.K. Rao, P.R. Nott, S. Sundaresan, An Introduction to Granular Flow, Cambridge University Press, New York, 2008.

[50] R.M. Nedderman, Statics and Kinematics of Granular Materials, Cambridge University Press, New York, 2005.

[51] W.G. Nan, M. Ghadiri, Y.S. Wang, Analysis of powder rheometry of FT4: effect of particle shape, Chem. Eng. Sci. 173 (2017) 374–383.

[52] H.A. Barnes, A Handbook of Elementary Rheology, University of Wales, Aberystwyth, 2000.

[53] C.K.K. Lun, S.B. Savage, D.J. Jeffrey, N. Chepurniy, Kinetic theories for granular flow: inelastic particles in Couette flow and slightly inelastic particles in a general flowfield, J. Fluid Mech. 140 (1984) 223–256.

[54] W. Losert, L. Bocquet, T.C. Lubensky, J.P. Gollub, Particle dynamics in sheared granular matter, Phys. Rev. Lett. 85 (2000) 1428–1431.

[55] Q. Zhang, K. Kamrin, Microscopic description of the granular fluidity field in nonlocal flow modeling, Phys. Rev. Lett. 118 (2017), 058001.

[56] H. Eyring, Viscosity, plasticity, and diffusion as examples of absolute reaction rates, J. Chem. Phys. 4 (1936) 283–291.